THE JOURNAL OF PHYSICAL CHEMISTRY C

pubs.acs.org/JPCC Article

Ultrafast Photocurrent and Absorption Microscopy of Few-Layer Transition Metal Dichalcogenide Devices That Isolate Rate-Limiting Dynamics Driving Fast and Efficient Photoresponse

Kyle T. Vogt, Su-Fei Shi, Feng Wang, and Matt W. Graham*

Cite This: J. Phys. Chem. C 2020, 124, 15195−15204 Read Online

ACCESS | Metrics & More | Article Recommendations | Supporting Information

ABSTRACT: Despite inherently poor interlayer conductivity, photodetectors made from few-layer stacked 2D transition metal dichalcogenides (TMDs) such as WSe_2 and MoS_2 often yield a desirable fast (≤∼90 ps) and efficient (ϵ > ∼40%) photocurrent response. To unambiguously separate the competing electronic escape and recombination rates, we combine ultrafast photocurrent (U-PC) and transient absorption (TA) microscopy methods. U-PC and TA kinetics obtained on WSe_2 photodetectors yield matching interlayer electronic escape times that accelerated from ∼1.6 ns to 86 ps with the applied *E*-field. These ultrafast rates predict the actual device PC efficiencies realized of 40−45%. The roughly linearly increasing electronic escape rates with applied voltage in TA and U-PC decay kinetics both give out-of-plane electron and hole mobilities of 0.129 and 0.031 $cm^2/(V\ s)$, respectively, in WSe_2. Above ∼10^{12} photons/cm^2 incident flux, defect-assisted Auger scattering greatly lowers the efficiency by trapping carriers at vacancy defects. Both TA and PC spectra identify a metal vacancy subgap peak with 5.6 ns lifetime as one primary trap capturing carriers as they drift between layers. TA and U-PC microscopy independently provide the kinetics of electronic escape and recombination that determine PC device efficiency. For few-layer TMD devices, this simple rate law further predicts the observed nonlinear in PC dependence over a 10^5 range of incident power.

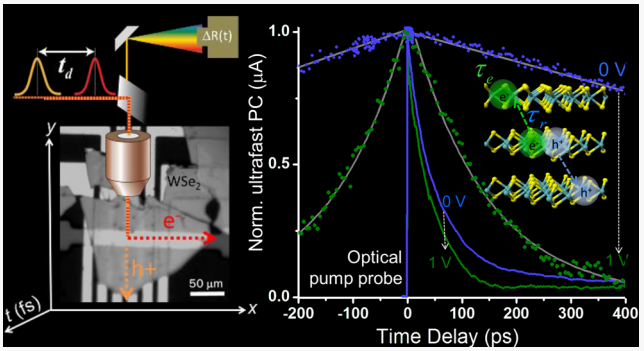

I. INTRODUCTION

Photodetectors made from few-layer stacked, semiconducting 2D transition metal dichalcogenides (TMDs) like WSe_2 and MoS_2 can have fast, sub ∼100 ps response time and efficient collection with internal quantum efficiencies (IQE, ϵ) of photocurrent (PC) often exceeding 40%.[3−5] In Figure 1a, the photodetector shown works by employing a parallel plate sandwich device geometry with a thin top-contact that uses either the built-in or applied voltage (V_A) to collect photoexcited electrons and holes. The stacked layers of WSe_2 or MoS_2 are only weakly coupled by van der Waals forces, resulting in very poor out-of-plane conductivity. To reconcile such weak interlayer coupling with previously reported high PC-IQE and fast photoresponse, this work isolates the competing kinetics pathways of carrier recombination and interlayer escape in few-layer stacked TMD devices.[1,2,5,6]

Measuring the electronic escape rates associated with PC collection remains challenging owing to complex intraband scattering and defect-assisted Auger recombination in van der Waals materials like few-layer TMDs.[7−9] Presently, there exists no reliable *in situ* method that isolates the effective linear recombination rate (τ_l^{-1}) from electronic escape ($\tau_{e/h}^{-1}$) rate in the ultrafast regime. Transport-based measurements lack the required time resolution, while purely optical ultrafast measurements provide a convoluted weighted average of all dynamics, offering no selectivity for rate components that contribute to PC production.[10] The high PC-IQE and nonlinear relaxation kinetics associated with TMDs give a nonlinear reduction in PC that can be time resolved together with purely optical measurements like transient absorption (TA) to isolate these carrier extraction mechanisms and rates.

Even under low incident flux and continuous wave (CW) excitation, the interlayer electronic dynamics in TMDs are often dominated by defect-assisted Auger scattering that localizes photocarriers at subgap vacancies and defects.[11−13] For example, one of the many defect-assisted Auger recombination processes is depicted in Figure 1c (inset) by electron−electron scattering to a subgap defect state with defect density, n_D. Such interactions have a rate coefficient, γ, and a kinetic rate, $R \propto n^2 n_D$ that scales nonlinearly with electron or hole density, *n*. Prior optical ultrafast studies show such Auger recombination kinetics

Received: March 25, 2020
Revised: June 7, 2020
Published: June 18, 2020

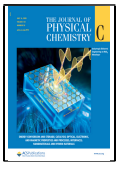

Downloaded via OREGON STATE UNIV on February 12, 2021 at 18:36:19 (UTC).
See https://pubs.acs.org/sharingguidelines for options on how to legitimately share published articles.

ACS Publications © 2020 American Chemical Society

https://dx.doi.org/10.1021/acs.jpcc.0c02646
J. Phys. Chem. C 2020, 124, 15195−15204

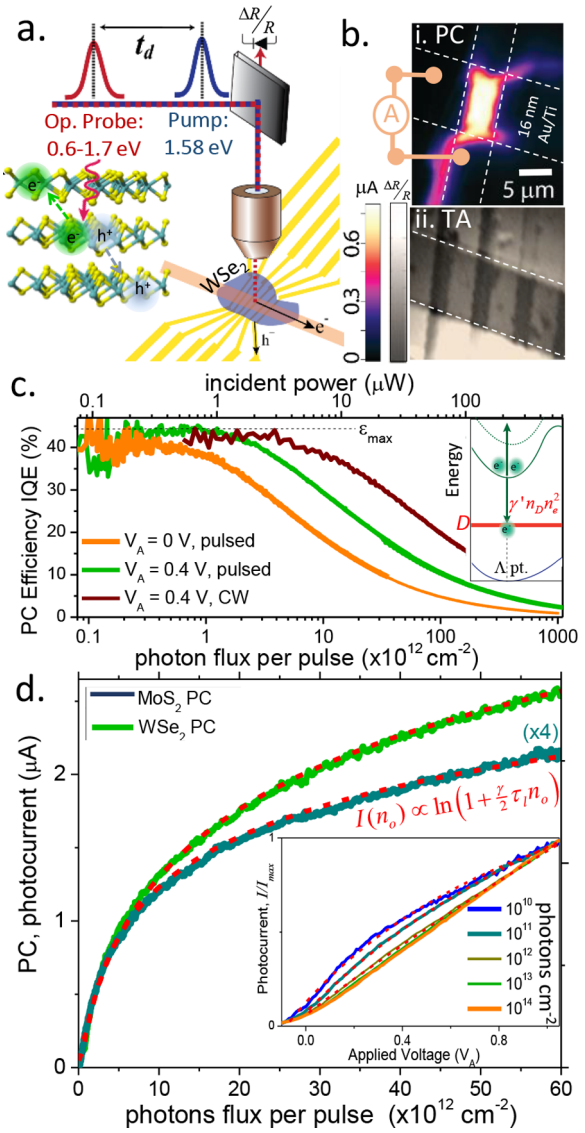

Figure 1. Nonlinear TMD photocurrent kinetics. (a) Experimental setup measuring ultrafast photocurrent (U-PC, $\Delta I(t, V_A)$) and transient absorption (TA, $\Delta R(t, V_A)$) response for the few-layer WSe_2 photodetectors shown. (b) U-PC and TA scanning microscopy maps show PC-active region of device. (c) Device PC-IQE decreases with photon flux for both pulsed and CW-illumination. (Inset) diagram showing Auger electron−electron scattering to defect state (D). (d) PC power dependence for WSe_2 (green, 0.4 V) and MoS_2 (blue, 0.5 V) fits to eq 4 (red dashed lines). (Inset) fits to normalized PC V_A-scans show the curvature is predicted by Auger effect in eqs 4 and 5.

dominate kinetic relaxation in few-layer TMDs at most pulsed and CW incident powers.[14−16] The full description of the fast electronic thermalization within the indirect-gapped band structure of WSe_2 requires even more complex kinetic rate models.[17−18] While such complex rate laws rationalize the multicomponent relaxations observed in optical TA-based measurements, it remains unclear which kinetic processes are practically relevant to PC generation and the overall device response time.[13,19] Here, we analytically test the adequacy of simpler kinetic rate models and identify which kinetic rates are sufficient to predict the net PC measured and response time in few-layer TMD-photodetectors.

By combining ultrafast photocurrent (U-PC) with transient absorption (TA) microscopy, this work identifies bottleneck mechanisms that intrinsically limit the maximum PC-IQE achievable in few-layer TMD photodetectors. Unlike TA, the U-PC response is time-integrated and may be selective for ultrafast dynamics limiting PC extraction.[2,5,20,21] However, this assumption is untested and it remains unclear how to extract first-principle kinetics from an U-PC transient reduction in photocurrent. To understand how the *E*-field-dependent U-PC kinetic decay is connected to first-principle kinetics, TA microscopy is also collected synchronously. Together, these *purely optical* and *purely electronic* detection regimes, predict similar ultrafast electronic escape times and furnish PC-generation mechanisms for TMD-based photodetectors.

II. METHOD DETAILS

II.A. Device Preparation. Efficient photodetectors using a few layers of TMD material are fabricated on the basis of designs inspired by previous works.[1,2,5] Gold contact pads (150 nm thick) are patterned on a silicon wafer. Both WSe_2 and MoS_2 were mechanically exfoliated and inspected optically to classify thickness. This was confirmed by atomic force microscopy (AFM) in the Supporting Information. Optimal thicknesses ranged from 50 to 100 layers such that >80% of incident light is absorbed, but the mean path for electron escape is short enough to efficiently collect photocarriers.[1,4] TMD samples were then spun-cast with methyl methacrylate (MMA) polymer, transferred mechanically onto the gold electrodes, and released thermally after careful cleaning steps optimize contacts. Optically translucent metallic 16/2 nm Au/Ti layers formed excellent top contact with the exfoliated TMD flake on a subset of devices fabricated. Each device had six distinct ∼10 × 5 μm regions shown in Figure 1a, each of which generates a uniform PC-response such as shown in Figure 1b, providing the exfoliated TMD layers make good electrical contacts. Eight independently working devices with strong, uniform PC response were studied, and all gave similar amplitudes after the stacking-layer thickness was corrected. Only devices generating multiple, uniform strong PC signal such as shown in Figure 1b were used to help decouple any weak Schottky barrier contributions to the otherwise strong PC response observed.

II.B. Ultrafast Photocurrent (U-PC) and Transient Absorption (TA) Microscopy. The photocurrent is collected by low-profile RF probes on micromanipulators beneath a high NA refractive or reflective objective of a home-built scanning confocal photocurrent microscope. In each case, the active photocurrent generated was formed by the overlap of the contacts; this forms a ∼10 × 5 μm region that generates a large, uniform photocurrent map such as shown in Figure 1b. This scanning photocurrent geometry is modified to accommodate simultaneous TA and U-PC measurements. Specifically, a linear delay stage is added to control the relative timing of the two incident laser pulses. One pulse is 780 nm and the other is 810 nm to prevent optical interference contributions to U-PC and still resonantly excite the optical gap of few-layer WSe_2 devices. All beams are aligned in a collinear geometry before a piezo scanning mirror (PI, #S-334.2SL) and coupled into the microscope (Olympus BX-61WI) using 4f scanning geometry. Both U-PC and TA microscopy signals are collected as a function of delay time using lock-in amplifiers and amplitude modulation of the two beamlines shown in Figure 1a. The ultrafast photoresponse was demodulated by either single or difference frequency chopping mode. Incident-photon-flux-dependent measurements used a motorized polarizer−wave-

https://dx.doi.org/10.1021/acs.jpcc.0c02646
J. Phys. Chem. C 2020, 124, 15195−15204

plate combination to study the TA and PC response continuously over a wide $\sim 10^{10}$ to 10^{15} photons/cm^2 continuous range. Using an Ithaco or Zurich Instrument current preamplifier and lock-in detection of the PC signals, the signal-to-noise was optimized for power-dependent and U-PC kinetics.

After resonant optical excitation of the K_A-point transition, the transient spectra and kinetics were measured using confocal scanning U-PC and TA microscopy methods.[20,22] Collinear pump and probe pulses were obtained from two independently tunable outputs of an ultrafast Ti:sapphire oscillator (Coherent Chameleon Ultra II, 80 MHz) pumping an optical parametric oscillator (APE-Compact). Unless specified, all measurements employed a nondegenerate excitation of the K_A-point optical gap near 780 nm, centered in a few-layer WSe_2 device. For spectrally resolved TA, a white-light supercontinuum probe was used to capture transient spectra. Cross-correlation of the pump and probe after the objective yielded a pulse duration of about 160 fs.

After a mechanical delay stage, both the pump and the probe beams were aligned in a collinear geometry, raster-scanned by piezo-scanning mirror, and coupled into a confocal scanning microscope via an Olympus 50XIR, achromatic objective (NA = 0.65). TA signals were detected by measuring the probe beam with a TE cooled InGaAs detector connected to a Zurich HF2-LI lock-in amplifier with a current preamplifier. The pump beam was modulated at 25 kHz using an acousto-optical modulator (Gooch and Housego). This enables high-frequency lock-in detection of the differential reflectivity, $\Delta R/R$, which for resonant excitation is taken a approximately proportional to the transient hot carrier carrier density, $\frac{4}{n^2-1}\Delta n_{e/h}(t_d, E_{pr}, V_A)$, within the resonant probe energy, E_{pr}.[23,24] Frequency was swept to ensure beam modulation frequency did not impact PC measured. Appropriate optical filters or Acton monochromator were used in front of the detector to block the pump beam and the select probe spectral window. The pump and probe spot sizes on the sample were determined to be ~ 1.5 μm, by fitting to a confocal scanning reflection profile of lithographic gold pad edges. For photocurrent-based U-PC measurements, the excitation pulses are fixed at $\sim 0.5 \times 10^{12}$ photons/cm^2 and 295 K unless noted otherwise.

III. RESULTS AND ANALYSIS

III.A. Nonlinear TMD Photocurrent Response. Using the fabricated photoconductive devices illustrated in Figure 1a the AC-photocurrent response was collected from both WSe_2 and MoS_2 devices using a raster scanning geometry of a pulsed (160 fs) or continuous wave (CW) laser. The roughly diffraction-limited spot is parked in the device center and is resonant with the lowest, K-point transition. In Figure 1b*i*, scanning PC microscopy spatial maps of a 67-layer WSe_2 device shows strong, uniform PC over the sandwiched regions that is 2−3 orders of magnitude greater than any edge-PC signals around the peripheral leads. The corresponding TA scanning microcopy map shown in Figure 1b*i* is sensitive to the carrier population remaining after at pulse delay time, $t_d = 1$ ps between pump and probe pulses resonant with the optical gap. Using these scanning maps, a 0.9−1.4 μm laser spot size was localized on the device center for all PC and TA measurements.

The PC internal quantum efficiency (IQE) for pulsed excitation can be defined as the ratio of the electrons collected to photons absorbed, $\epsilon \cong n_{PC}/n_{abs}$. For our few-layer TMD devices nearly all photons (>85%) are absorbed in our resonant excitation regime. Parts c and d of Figure 1 show the WSe_2 and MoS_2 device PC-IQE drops as the incident photon flux increases by $\sim 10^4$ (see Supporting Information S.2 for IQE and EQE calculation details). This precipitous drop suggests nonlinear rate kinetics are required to predict the PC amplitude above a $\sim 10^{11}$ photons/cm^2 threshold. This threshold photon flux in PC-IQE further increases by a factor of ~ 10 going from $V_A = 0$ (orange line) to 0.4 V (green line) and also for continuous wave (CW) illumination 0.4 V (red line).[1,2] This shift is understood by noting the Auger recombination rate, $R \propto n^2 n_D$, increases with mean carrier density in the device. This nonlinear recombination is more likely when electron drift velocity slows as $V_A \to 0$, causing the mean number of photocarriers in the device to increase. While the nonlinear PC dependence in Figure 1c,d has been previously attributed to Auger recombination processes,[2,18] there exists no reliably proven analytic model linking the PC to the optical responses in such few-layer TMD materials.

In agreement with the original few-layer TMD device studies by Yu et al.,[1] panels c and d of Figure 1 show a highly nonlinear PC response for both resonant CW and pulsed excitation in WSe_2 and MoS_2 devices. This motivates the inclusion of slow defect-assisted scattering Auger processes in our kinetic model for PC. Previously, Wang et al. showed that the nonlinear response had contributions from both fast Auger recombination with rate $\gamma_f n$ and slower interlayer defect-assisted Auger recombination processes with rate γn, where n is either the electron or hole density.[11,25] Fast Auger processes occur on a time scale commensurate with the interlayer electron−hole separation time, τ_d.[26] The rate law for slower defect-assisted Auger processes is written as $R = \gamma n^2$, where $\gamma = n_D \gamma'$ and scales linearly with the constant metal or dichalcogenide vacancy defect concentration.

To model the nonlinear PC response in few-layer WSe_2 and MoS_2 photodetectors, we first consider a simplified kinetic rate law of the PC-efficiency-limiting rate processes. We approximate the total linear rate, τ_l^{-1}, involved in PC generation as the sum of the electron/hole net escape rate, $\tau_{e/h}^{-1}(V_A)$, and linear recombination rate, τ_r^{-1}. In this approximation of ignoring spatial- and valley-dependent dynamics, the rate law for the time evolution of electron or hole photocarriers density $n(t)$ is simply

$$\frac{dn}{dt} = n_o \delta(t) - \frac{n}{\tau_l} - \frac{1}{2}\gamma n^2 \tag{1}$$

$$n(t, n_o) = n_o \left[e^{t/\tau_l} + \frac{\tau_l \gamma n_o}{2}(e^{t/\tau_l} - 1) \right]^{-1} \tag{2}$$

The above solution to the rate law predicts that carrier density grows nonlinearly with initial photocarrier density, n_o, which is further taken to be proportional to incident power.[27] In the low carrier density limit ($\gamma n_o \cong 0$), eq 2 gives the carrier density, $n(t)$, growing linearly with initial carrier density, n_o (and incident photon flux). This purely linear PC-response region is clearly consistent the constant IQE plateau region shown in Figure 1c at sufficiently weak incident power. Similarly, in Figure 2b both PC signals evolve from a linear to nonlinear scaling with increasing photon incident flux. Figure 2b also plots TA deferential reflectivity power dependence for the WSe_2 (orange line, right axis) on a square root scale and shows the power-scaling fits well to eqs 1 and 2 (dashed red line).

To test if eq 1 can also predict the interlayer PC response from few-layer TMD photodectors, Figures 1d and 2b fit the integrated PC response over a 10^5 change in photon flux,

https://dx.doi.org/10.1021/acs.jpcc.0c02646
J. Phys. Chem. C 2020, 124, 15195−15204

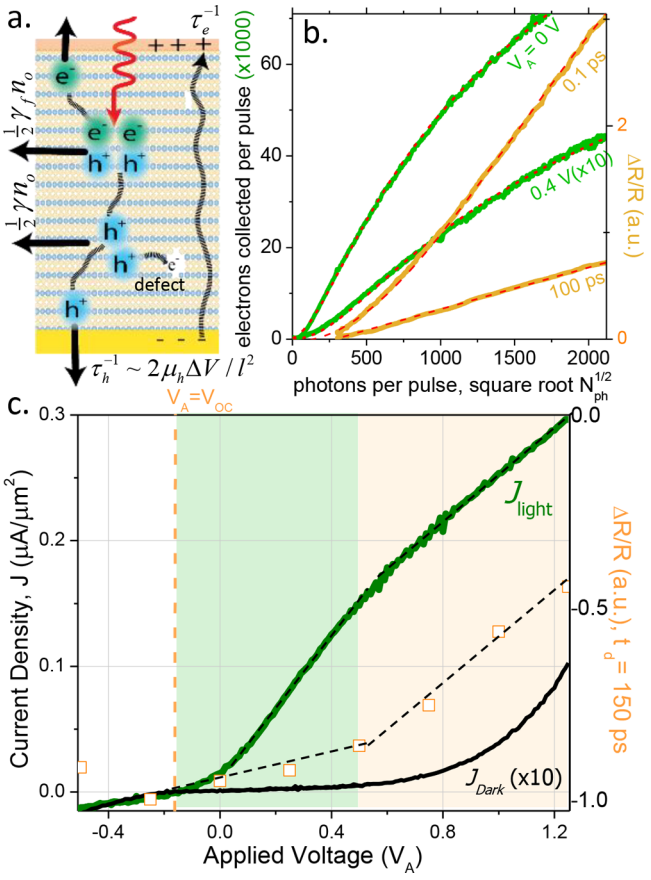

Figure 2. PC vs absorptive kinetic-model predictions. (a) Device cross-section depicts both PC and photoconduction nonlinear decrease owing to fast (γ_f) and slow (γ) Auger recombination to WSe_2 vacancy traps. (b) PC (green) and TA amplitude (orange) plotted vs square root of the incident photons per pulse shows the nonlinear trend is well-modeled by the red dashed lines fits to eq 4 for PC and eq 2 for TA. (c) Resonantly excited J_{light} (green) and J_{dark} (black) current density V_A dependence plotted with TA amplitude for t_d = 150 ps (orange squares, right-axis). Shading highlights a quasi-linear regime separating the PC (green) from photoconduction (orange) dominated collection regimes.

showing remarkable agreement. The integrated photocurrent density, $J_{e/h} = -D_{e/h}\frac{dn}{dx}$ of electrons or holes is a spatial transport process traditionally defined through the diffusion coefficient, $D_{e/h}$, and any driving applied voltage.[7] Alternatively, for few-layer devices we instead approximate $J_{e/h}$ in the time domain by integrating time-dependent carrier density, $n(t)$, given by in eq 2 and doing a time average over the mean electronic escape time, $\tau_{e/h}$, to get

$$J_{e/h}(n_o) = \frac{-e}{\tau_{e/h}} \int_0^\infty n(t)\, dt \tag{3}$$

$$= \frac{-e}{\tau_{e/h}\tau_1\gamma} \ln[1 + \tau_1\gamma n_o/2] \tag{4}$$

This yields a simple, but highly predictive, expression showing how the PC collected depends nonlinearly on the initial photoexcited carriers created (n_o). In Figures 1d and 2b, the red-dashed lines are fits to eq 4. We see excellent agreement with PC spanning 5 orders of magnitude of photon-flux dependence for both 56 nm-thick WSe_2 (green line) and 43 nm-thick MoS_2 (blue line). The highly predictive nature of eqs 2 and 4 suggest the simple rate law in eq 1 sufficiently captures the rate-limiting kinetics germane to PC collection. In section III.B, we test this assumption by extracting electronic escape rates from U-PC and TA ultrafast kinetics.

Previously, the photogenerated carrier escape rates, $\tau_{e/h}$, have been previously approximated using the drift velocity, $v_D = -\mu_{e/h}E \cong l/\tau_{e/h}$, where $\mu_{e/h}$ is the out-of-plane electron or hole mobility and l is the mean distance to escape.[2,21] In the thin sandwich device geometry shown in Figure 1a, the perpendicular E-field is approximated as $E \sim |V_A - V_{OC}|/L = \Delta V/L$ (see Supporting Information for justification), where V_{OC} is the device open-circuit voltage. Solving for the electronic escape time, one obtains

$$\tau_{e/h}^{-1}(V_A) = \frac{\mu_{e/h}|V_A - V_{OC}|}{lL} \tag{5}$$

where l is the mean distance of photocarrier transport to the electrical contacts. AFM of the WSe_2 device shows the total TMD-layer thickness is L = 56 nm. In Figure 1d (inset), by combining eqs 4 and 5, we further predict the PC curvature change with V_A (red line fits) over the 10^4 range of photon flux shown. Thus, both the expected linear scaling region of $J_e \propto |V_A - V_{oc}|$ and the nonlinear scaling regions can be accounted for by adding the flux-dependent nonlinear recombination Auger rate to our PC-kinetics response model.

As depicted in Figure 2a by the dashed arrows, TMDs placed between capacitively matched contacts have two modes of operation. Either the photoexcited electron−hole pairs are extracted (for low applied voltage, V_A) as a PC or a photoconductive current between contacts is optically induced as the diode-like response turns on at higher V_A. In Figure 2c, the green trace is the illuminated current density, J_{light}, and shows an inflective change near 0.55 V. For comparison, the dark current, J_{dark}, plotted is ∼100 times smaller than J_{light} and exhibits diode-curve-like behavior. As PC signals shown are detected by using lock-in detection, the weak, J_{dark} response is removed from all our signals to isolate only the photoresponse. There are two quasi-linear regimes in Figure 2c (dashed black line fit) delineated by the green or orange background shading. Each region corresponds to PC dominated by photoextraction or photoconduction, respectively. The orange squares on the right-axis of Figure 1d show the amplitude of the TA differential reflectivity amplitude, $\Delta R(V_A)/R$ for t_d = 150 ps. Interestingly, the purely optical TA signal also shows two quasi-linear regions, tracking the PC electronic signal closely.

When photoexcited carriers are directly extracted as a PC, prior works and electric field simulations (see Supporting Information S.1) suggest the mean escape distance is approximately half the WSe_2 thickness, $l \cong L/2$.[2] Conversely, in photoconduction mode shown in Figure 2a, the electronic carriers must travel the mean device thickness. Figure 2c suggests the PC response evolves to a photoconductive dominated response as the applied voltage, V_A, is swept from the open-circuit value, V_{OC} = −0.089 to 1.30 V. One also observes this effect by the fluency-dependent inflection in Figure 1c (inset). Both results suggest below ∼5 × 10^{12} photon/cm², PC collection becomes favorable over photoconduction. In the next section, the associated dynamic rates driving the PC response are investigated using a novel ultrafast kinetic analysis by on-chip PC and TA microscopy.

III.B. Connecting PC and TA Ultrafast Kinetics to Device Efficiency and Response Time. In section III.A, a simple kinetic rate law (eq 1) predicts both the photon-flux-

https://dx.doi.org/10.1021/acs.jpcc.0c02646
J. Phys. Chem. C 2020, 124, 15195−15204

dependent PC and TA absorption amplitudes better than any previsouily used power-law approximation. However, extraction of kinetic rates pertinent to the PC response of few-layer TMDs further requires sub-100 ps time resolution and selectivity for PC generating kinetics. To accomplish this, Figure 3a plots the ultrafast photocurrents (U-PC) response measured with the TA response in Figure 3b. Both TA and U-PC kinetics accelerate markedly with increasing applied voltage, V_A, from near-zero at V_{OC} to 1.3 V. Unlike in the U-PC decay, many of the kinetic decay components in TA appear invariant to V_A.

Prior works applying U-PC to graphene, carbon nanotubes, and 2D TMDs suggest U-PC is sensitive to the dominant ultrafast kinetic rate-processes that intrinsically limit PC collection.[2,5,18,20,21,28] Figure 3a shows the normalized U-PC kinetics markedly accelerate with increasing applied voltage, consistent with faster carrier extraction from the device. Similar fast U-PC kinetics on WSe_2 photodetectors were first reported by Massicotte et al. and Vogt et al.[2,5] However, there was no clear method to connect the numerical fits to the inherently nonlinear first-principle kinetics that drive U-PC responses such as those in Figure 3a.

Motivated by the highly predictive PC-fits in Figures 1d and 2b to eqs 3 and 4 (red dashed lines), a related U-PC response function is proposed by direct piece-wise integration of $n(t)$ about the delay time, t_d,

$$\Delta J_{e/h}(t_d) = \frac{e}{\tau_e}\left(\int_0^{t_d} n(t, n_o)\, dt + \int_{t_d}^{\infty} n(t, n_o + n(t_d))\, dt\right) \quad (6)$$

After evaluating the integrals using eq 3 for $n(t)$, eq 6 fits U-PC kinetics in Figure 3a with only two free-parameters (solid color lines), an electronic escape rate and a defect-assisted Auger recombination constant, γ. Moreover, the above U-PC response function correctly captures the kinetic decay accelerating with V_A better than exponential fits assumed in other recent U-PC studies.[2,22] All data and simulation are normalized to peak maximum to compare dynamics (see Supporting Figure S3 for examples of uncorrected raw data). As such, all U-PC kinetic fits like in Figure 3a also require subtraction of the constant background PC signal, given by $2\int_0^{\infty} n(t, n_o)\, dt$.

As an independent test the U-PC response function proposed in eq 6, we compare the U-PC rates extracted in Figure 3a against concurrently obtained, faster-looking TA kinetics. Figure 3b shows TA microscopy kinetics, also pumped and probed about K_A point. The TA relaxation increases markedly with applied voltage (V_A), but only in the second decay component. The inset of Figure 3b clearly shows the TA signal-amplitude strongly decreases with V_A, but only for $t_d \sim 70-150$ ps range associated with the second TA decay lifetime. The other decay components at shorter and long delay times are largely invariant to the applied field.

As one might expect, the slowest TA relaxation in Figure 3b was not observed for $V_A = 0$, but instead at the open-circuit voltage, V_{OC}, where no net-PC is collected. A least-squares deconvolution fit of the kinetics at $V_A = V_{OC}$ using eq 2 gives $\tau_r = \tau_l \cong 92$ ps for the linear recombination rate. The τ_r lifetime was not observed to change with incident photon flux. Owing to the high PC-IQE (up to 44%) of our WSe_2 photodetectors, the accelerating TA kinetics in Figure 3b correspond to either the carrier extraction time or the carrier lifetime for photoconduction. Figure 3c (orange squares) plots the TA electronic escape rates obtained from the rate kinetic relation, $\tau_{e/h}^{-1}(V_A) \cong$

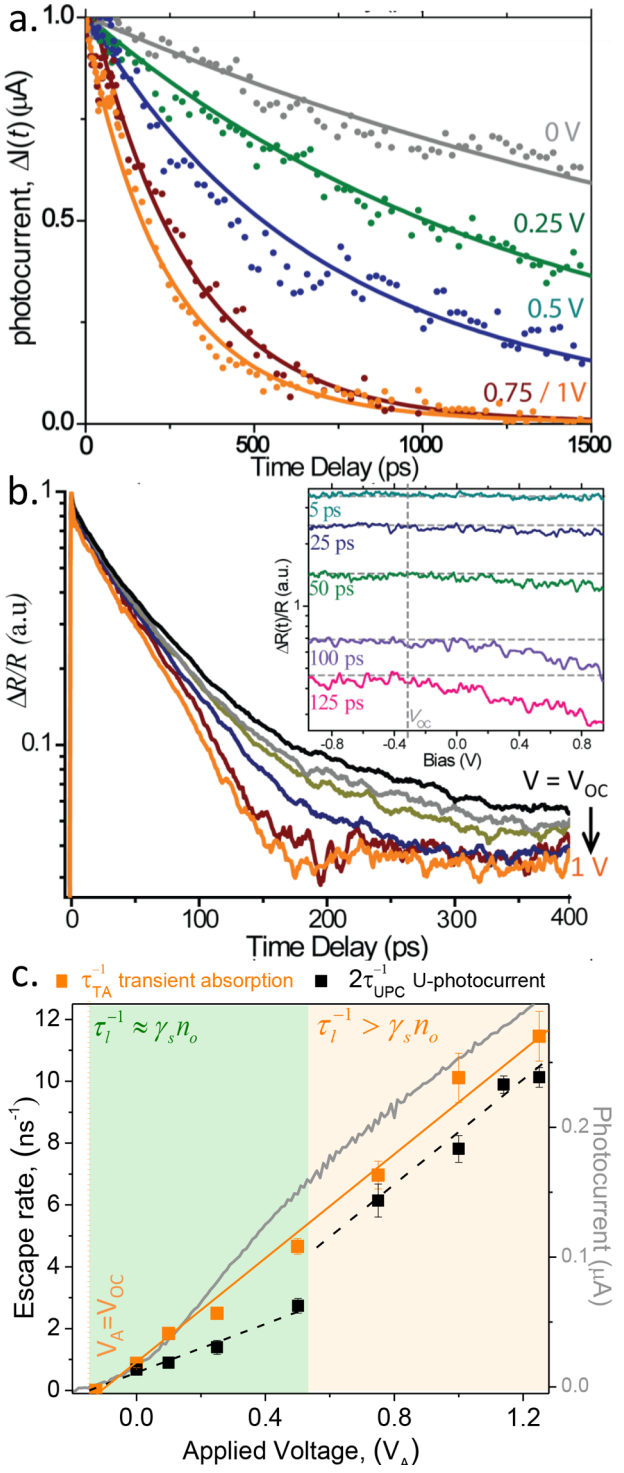

Figure 3. Ultrafast carrier escape, optical vs PC responses. (a) Normalized U-PC response from WSe_2 accelerate with increasing V_A. Solid lines are fits to U-PC response function eq 6. (b) Concurrently measured resonant TA kinetics also accelerates in the second decay component only as V_A is increased from V_{OC} to 1 V, the second component. (Inset) TA amplitudes decrease as electrons escape. (c) Both TA rates (orange) and U-PC kinetic rates (black) both increase linearly with applied voltage. Interestingly, the overall device PC response (gray line, right axis) scales likewise. The slope of the linear fits of the TA and U-PC rate approximate WSe_2 mobility, $\mu_{e/h}$.

$\tau_l^{-1}(V_A) - \tau_r^{-1}$ and they increase linearly with V_A. Obtained by fitting of U-PC kinetics to eq 6, Figure 3c also overlays (black

https://dx.doi.org/10.1021/acs.jpcc.0c02646
J. Phys. Chem. C 2020, 124, 15195−15204

square) the concurrently measured $2\tau_{e/h}^{-1}$ photocurrent ultrafast rates. Both extracted U-PC and TA rates are plotted in Figure 3c, and both increase roughly linearly with V_A. The solid lines are fits to eq 5, and the resulting slope provides an estimate of the electron and hole mobilities (summarized in Table 1).

Table 1. Example Figures of Merit of Ultrafast Rates Extracted from a Few-Layer WSe_2 Photodetector[a]

method	V_A	$\tau_{e/h}$	τ_r	τ_l	v_d	$\mu_{e/h}$	ϵ_{max}
(1) TA_e	V_{OC}	0	92	92	0		
($l \cong L/2$)	0	1258		57	24		
	0.75	148		86	180		
	1.25	86		44	300	0.13	0.52
(2) U-PC_e	0.75	326			170		
($l = L$)	1.25	196			290	0.12	0.43
(3) U-PC_h ($L/2$)	0.5	714			80	0.031	
(4) device PC	0						0.43
	1.25						0.44
(units)	V	ps	ps	ps	m/s	$cm^2/(V\ s)$	

[a] μ_{eh} are obtained from linear slopes of Figure 3c by eq 5. U-PC decay rates predict the actual device max IQE, ϵ_{max} slightly better than TA-derived escape rates.

In the time domain, PC-generation efficiency (ϵ) can be approximated by a ratio of competing kinetic rates given as $\epsilon \cong \frac{\tau_{e/h}^{-1}}{\tau_{e/h}^{-1} + \tau_r^{-1} + \gamma' n_D n}$. For low photon fluence, when the defect-assisted Auger scattering rate is small, the PC-IQE is $\epsilon_{max} \cong \frac{\tau_{e/h}^{-1}}{\tau_{e/h}^{-1} + \tau_r^{-1}}$. For few-layer WSe_2, nonlinear Auger contributions are generally slow or very fast. As a result, both U-PC and TA dynamics were largely independent of photon flux over the time scale reported for electronic escape. The PC-IQE figures of merit obtained from Figure 3c, are summarized in Table 1. At ϵ_{max} = 43%, the U-PC extracted rates predict the conventionally measured device IQA, $\epsilon_{max} = n_{PC}/n_{abs}$ = 44%, somewhat better than the TA rate prediction of 52%. The higher efficiency predicted by TA may come from an overestimate of the actual electron drift length as $l \cong L/2$. This approximation is not needed for U-PC as the electrons generally travel the full TMD thickness in photoconduction mode. This justifies why rates in Figure 3c are plotted as $2 \times \tau_{e/h}^{-1}$, reflecting the longer distance traversed.

Figure 3 highlights the remarkable similarity between the *E*-field-dependent ultrafast rates for the purely optically derived TA (orange squares) and the electrical U-PC rates (black squares). The agreement of optical and electronic responses above V_A = 0.3 V suggests the U-PC response function proposed in eq 6 correctly retrieves the rate-limiting escape kinetics driving PC-generation in few-layer TMD devices.

III.C. Discussion. WSe_2 in-plane conduction can approach >350 $cm^2\ V^{-1}\ s^{-1}$, whereas the out-of-plane conduction between stacked layers is generally ~10^4 smaller.[3,29] In many case, devices made using the this out-of-plane conduction are more efficient than the single-layer in-plane conducting devices.[3] The large resonant absorption of multilayer WSe_2, short mean distance ~20−30 nm to extraction, and long recombination times collectively help realize the high PC-IQE we calculated from steady state and ultrafast rate in Table 1. Unfortunately, the high defect densities (n_D) common to TMDs negate this advantage owing to strong Auger recombination that impacts the PC response for incident powers above a few microwatts.

Various spectra (absorption, TA, and PC) of our 56 nm thick WSe_2 photodetector are plotted in Figure 4a and show many optical transitions that suggest our simple kinetic analysis using just one carrier density, $n_{e/h}$ in eqs 1−6 is insufficient. A full model of the relaxation pathways of resonantly excited WSe_2 would track transient electron and hole population at all low-lying symmetry points, Γ, Λ, *K*, and subgap defect vacancy population at D. Such complete kinetic models have been the subject of many transient optical absorption and time-resolved photoluminescence studies, but it is unclear if these more-complete kinetic models are needed to sufficiently explain photocurrent collection in TMDs.[11,30−34]

To examine the impact of assumptions made in our kinetic model of PC generation for few-layer WSe_2, let us first consider fast Auger processes. Prior optical ultrafast studies show TMD relaxation dynamics are dominated by defect-assisted Auger scattering (e-e, e-h, h-h) to subgap vacancy defect sites such as Se or W vacancies.[8,11,12,18,35,3637] During interlayer drift, Figures

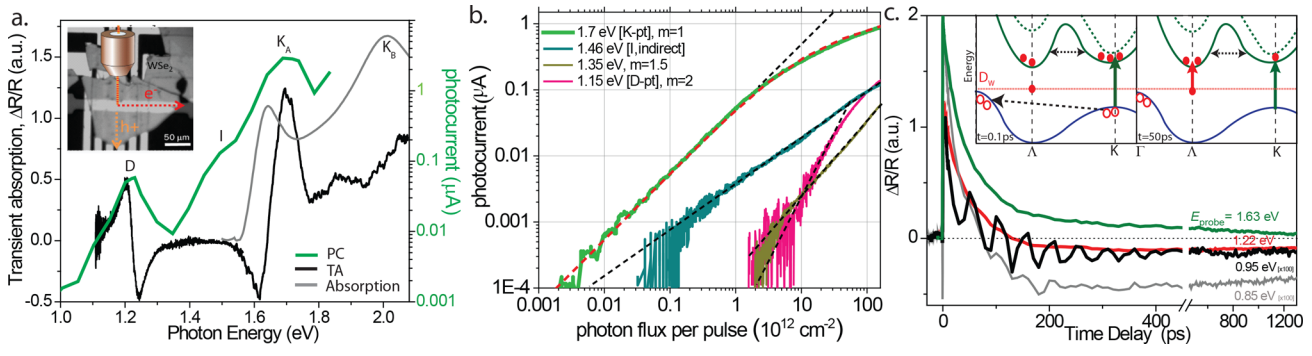

Figure 4. Defect mediated carrier relaxation. (a) Linear absorption (gray), PC (green, log-scale), and TA (black) spectrum at t = 0.5 ps for WSe_2. Below the optical bandgap at K_A, peaks are observed at the indirect-gap transition, I, and defect peak, D. (Inset) U-PC, and TA signals are collected simultaneously on the WSe_2 photodetectors fabricated. (b) As excitation photon energy approaches the D-peak region of the subgap, the power dependence shifts from linear to quadratic (log−log scaling). Above the optical gap, the Auger-recombination kinetics in eq 4 (red dashed line) models the clear transition from linear to sublinear PC-response. (c) TA-kinetics for resonant pump, subgap probe are slower than the resonant case. A purely thermal response is suggested by analysis of the 44 ps beat oscillation as the thermal acoustic wave launched over the device thicknesses. (Inset) band-structure schematic of WSe_2 shows transient carrier populations at 0.1 and 50 ps. While TA in this work mainly probes thermalized electrons near the K_A (green arrow) or D (red arrow) transitions shown, U-PC is sensitive to the lower mobility hole-extraction (open circles).

https://dx.doi.org/10.1021/acs.jpcc.0c02646
J. Phys. Chem. C 2020, 124, 15195−15204

1 and 2 suggest defect-assisted Auger recombination dominates when the incident photon flux is sufficiently high (>10^{12} photon/cm^2). Fast Auger is further indicated by the strong square root scaling of the TA amplitude with the photon flux shown in Figure 2b.[17] After excitation, the electron−hole pairs dissociate at rate τ_d^{-1} or undergo fast-Auger scattering at rate $\gamma_f n_{eh}$ with a kinetic rate of electron−hole pairs (excitons) written as[38−43]

$$\frac{dn_{eh}}{dt} = n_{abs}\delta(t) - \frac{n_{eh}}{\tau_d} - \frac{n_{eh}}{\tau_r} - \frac{1}{2}\gamma_f {n_{eh}}^2 \quad (7)$$

At very short delay times, our TA kinetic decays show signatures of the above kinetic rate law associated with electronic scattering and dissociation. In the Supporting Information, Figure S3 photon-flux-dependent TA kinetics show the initial kinetics accelerate with the incident photon flux. Such effects only last a few picoseconds, far slower than the measured fastest interlayer electron escape time of 82 ps in this work.

In Figure 4a, we overlay the linear absorption (gray), TA (black), and PC (green) responses from our WSe_2 device over a 1.0−2.1 eV spectral range. Near 1.68 eV the integrated TA transient bleach and the linear absorption both peak at the resonant K_A-point transition corresponding to the optical gap. Unexpectedly, we also observe a subgap excited state absorption (ESA) peak centered at 1.21 eV in our TA spectrum. While this subgap peak was not present in our linear absorption, the PC spectrum in Figure 4a (green line, semilog scale) confirms the existence of subgap peak. This PC spectrum further has a labeled shoulder peak, I, that matches well the indirect bandgap of our WSe_2 at 1.53 eV.[33]

To understand the origin of PC and TA response observed with a D-peak at 1.21 eV, in Figure 4b we plot a PC laser flux power dependence for four excitation energies on log−log scaling. For the resonant excitation case at K_A, the red-dashed line fits to eq 4 remarkably captures the PC response over 5 orders of magnitude. It further clearly delineates the onset of nonlinear-PC response for WSe_2 devices at ∼10^{12} photons/cm^2 flux.[44,45] For subgap region excitation of the D-peak PC response at 1.15 eV, Figure 4b shows the subgap PC response is superlinear with a photon flux (slope of ∼1.9−2).[32,46] While direct optical excitation of defect states is generally not possible owing to momentum-matching restrictions, a weakly allowed two-photon excitation is proposed. Figure 3b supports a two-photon excitation by the characteristic quadratic increase in PC response that we observe only when the energy matching the ESA TA D-peak. Comparison with existing DFT simulations of WSe_2 with tungsten metal vacancy cells places this defect band near the valence-band maximum, as depicted in Figure 4c. Energetically, tungsten vacancies explain the subgap peak labeled D in Figure 3c better than selenium vacancy defects.[30,47,48]

The inset of Figure 4c schematically depicts the multilayer WSe_2 band structure dynamics at t_d = 0.1 and 50 ps. Energetically, the holes are preferentially scattered far out of the resonant spectral probe window to the Γ-point. This makes our resonantly probed TA predominantly sensitive to thermalized electron populations at the Λ and K conduction band wells. As holes have lower mobility in WSe_2, the PC is strongly impacted by the hole escape rate unless the device is in photoconduction mode. Accordingly, our U-PC escape rates plotted in Figure 3c at low applied V_A fit to eq 6 and the slope estimates the out-of-plane hole mobility of 0.031 cm^2/(V s). The hole mobility is ∼3−4 times smaller than the out-of-plane electron. This difference is consistent with the larger effective mass suggested by WSe_2 DFT band curvature near the valence band maximum at the Γ-point.[47,48] At V_A larger than ∼0.3 V the high-resistance WSe_2 device transitions to photoconduction mode where the U-PC kinetics are instead limited by the photoinduced-electron lifetime. In Figure 3c, the slope of both the TA and U-PC escape rates agree, giving identical estimates of the electron mobility of 0.128 cm^2/(V s). These time-domain values of the mobility agree reasonably well with literature transport-based out-of-plane mobility estimates for WSe_2.[13,48,49]

Figure 4c plots the relaxation kinetics now using subgap probe windows. For subgap E_{probe} energies below the D-peak resonance, the TA response is ∼<100 times weaker. We attribute the very long lifetime components of the signals in Figure 4c at 0.85 and 0.95 eV to the transient thermal response WSe_2. This is supported by the incidental presence of a strong TA beat period of 44 ps that further predicts a speed of sound of 2650 m/s in WSe_2, which is an order of magnitude faster than the interlayer electronic drift velocities, v_d, in Table 1.

Figure 5a helps complete the timeline for photoextraction by plotting the fluence-dependent TA kinetics for a 67-layer WSe_2 device using a pump and probe energy again resonant with the optical gap. The longest ground state recovery component fitted is ∼5.6 ns and is attributable to defect relaxation. This rate is further dependent on the Auger scattering rate populating these defects, as shown by the fluence-dependent kinetics in in Figure 5a. This coincides with the defect-assisted Auger recombination rate, γn, growing with the photon flux. Thus, at high photon flux there are more vacancy-trapped electrons reflected by an effective increase in defect lifetimes from ∼3 to 6 ns.

Panels b and c of Figure 5 summarize our primary TA and U-PC microscopy results by plotting both ultrafast signals as a function of time, space, and applied voltage. The spatial maps show a sequential, uniform relaxation of the transient PC and TA signals. Unlike TA microscopy, U-PC microscopy is confined to the overlap regions of the sandwiched contact regions shown by the yellow box. Lastly, in Figure 5d a cartoon timeline crudely depicts the dominant photocurrent generating pathways resolved with U-PC and TA, from light absorption to photocurrent collection. The combination of these methods provides the selectivity that isolates the PC-relevant kinetic rates of Auger recombination ($\gamma n(t)$), linear recombination (τ_r^{-1}), and mean escape rate, τ_e^{-1}. The primary mechanisms impacting the PC extraction efficiency in Figure 5d (and Figure 2a) are intralayer phonon-assisted carrier recombination, and Auger recombination of electrons and holes to subgap defect sites. However, the τ_r = 92 ps associated with largely phonon-mediated intralayer recombination (or perhaps contributions from fast Auger processes) fundamentally limits extraction efficiency at all the applied voltages examined here. Once the electron and hole are localized on separate layers, they can be extracted unless they encounter a defect site and undergo Auger recombination. Longer lifetime effects such as device TMD-electrode conduction rate and defect lifetimes seen in Figure 5a do not have any obvious impact on the U-PC kinetic response.

Comparing our representative results in Table 1 to related earlier works, Massicotte et al. reported that similar, graphene-sandwiched stacked WSe_2 devices with ϵ_{max} > 30% also had very similar fast picosecond electron escape times estimated from the U-PC decay.[2] For similar thickness WSe_2 devices, our rates extracted in Figure 3c closely match these earlier works.[2,5] For much thinner TMD stacks, Massicotte et al. report faster

https://dx.doi.org/10.1021/acs.jpcc.0c02646
J. Phys. Chem. C 2020, 124, 15195−15204

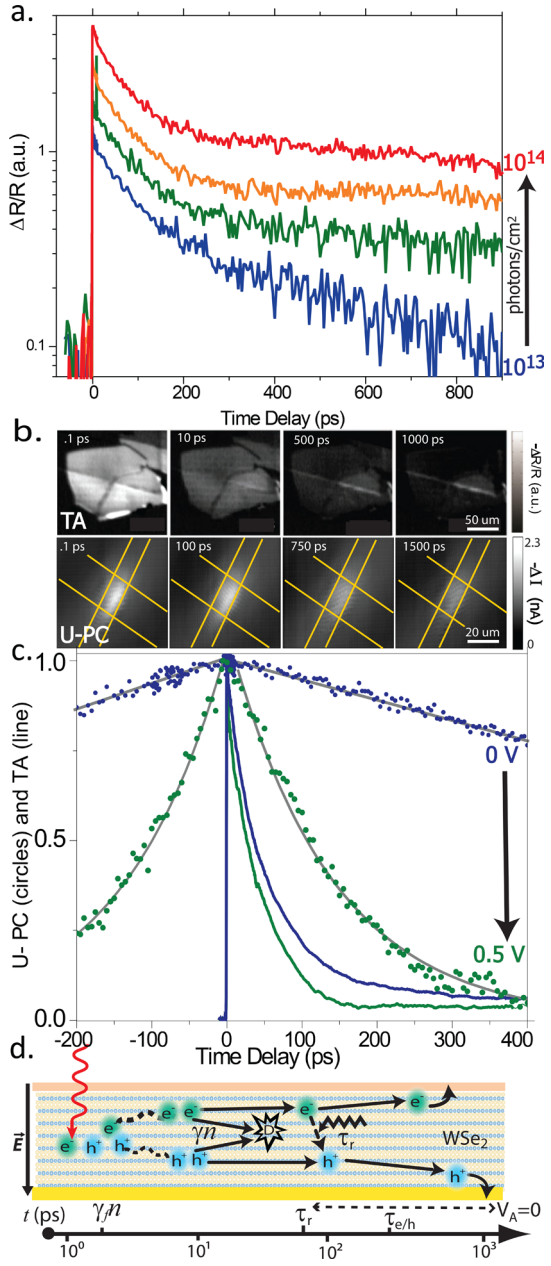

Figure 5. Ultrafast photoextraction timeline. (a) TA of a WSe_2 photodetector for E_{probe} = 1.62 eV. The longest lifetime component is associated with the relaxation of defect-trapped carriers and slows from ~3 to 6 ns TA at high photon flux. (b) Spatially resolved TA (top) and U-PC (bottom) kinetic maps effectively film the ultrafast electronic escape and recombination in the WSe_2 device. (c) Direct overlay of U-PC and TA kinetics at V_A = 0 (blue) and 1.5 V (green). Gray lines are analytic fits to the U-PC response function, eq 6, and provide Auger recombination and escape rates, $\tau_{e/h}$. (d) Summary timeline depicting efficiently limiting PC generation mechanisms in WSe_2, including e-h dissociation, defect-assisted Auger recombination, phonon-mediated recombination, and electron escape. Ultimately, the device PC efficiency is limited by the ~90 ps intralayer recombination time.

electronic extraction times (down to ~50 ps).[2] While the kinetic model in eqs 1 and 2 is crude compared to those applied in recent TA studies,[11,14,15,25] our model is still sufficient to fit both the PC amplitude and rate-limiting kinetics shown Figures 1 and 2 by the red-dashed line fits. The agreement between the U-PC rates and TA rates in Figure 3c suggests the U-PC response function extracts the correct escape time $\tau_{e/h}$ and first principle kinetics mechanisms seen in the purely optical response.[S0−S2] By isolating the ultrafast electronic escape rates, our synchronous TA and U-PC microscopy suggests a new, unconventional approach to screen new photonic materials before great expense is incurred on device prototyping.

IV. SUMMARY AND CONCLUSIONS

Photodetectors of few-layer semiconducting TMDs like WSe_2 have low out-of-plane mobility and strong defect-assisted Auger recombination even under CW excitation.[1,13] Nonetheless, recent studies of stacked WSe_2 show TMD photodetectors can be both efficient and have a fast rise time.[2,5] By combining *E*-field-dependent U-PC with TA microscopy, we identified the dominant kinetic bottlenecks inhibiting photocurrent efficiency for stacked few-layer TMD semiconductor photodetectors. As the applied voltage increases, both the TA and U-PC escape rates increase linearly together as $\tau_e^{-1} \propto |V_A - V_{OC}|^{-1}$, from $\tau_{e/h}$ = 86 ps to 1.6 ns. Using these rates, a simple kinetic rate model of carrier escape and recombination sufficiently models the device PC-IQE and nonlinear PC-power dependence over a 10^5 change in photon flux.

The origin of the U-PC rates extracted using the response function given by eq 6 was confirmed by the nearly identical synchronously obtained TA rates plotted in Figure 3c. The ratio of competing ultrafast rates extracted from TA and U-PC predicts an $\epsilon_{max} \cong 43\%$ (PC-IQE) and further suggests our TMD photodetectors are intrinsically limited by the intralayer 92 ps recombination time we extract at device open-circuit voltage. The ϵ_{max} obtained from the ulatrafast rates $\tau_{e,max}^{-1}$ and τ_r^{-1} match the actual 44% IQE we conventionally measured for WSe_2 devices in Figure 1b in the low photon-flux case where Auger recombination is suppressed. Both optical and electronic methods gave independently agreeing electronic escape rates that linearly grow with the applied field. In the plot of $\tau_e^{-1}(V_A)$ the slope provides out-of-plane electron and hole mobility estimates for WSe_2 of 0.129 and 0.031 $cm^2/(V\ s)$, respectively. The large absorption coefficient, short escape lengths, and the suppressed recombination of separated carriers help explain why WSe_2-based photosensors tend to be fast (<90 ps) and efficient despite such low out-of-plane carrier mobility. This combined U-PC and TA approach can now be extended to quantify how on-chip PC-extraction competes with recombination and trapping rates in many emerging photonic material systems.

■ ASSOCIATED CONTENT

Supporting Information

The Supporting Information is available free of charge at https://pubs.acs.org/doi/10.1021/acs.jpcc.0c02646.

Section S.1, electric field in WSe_2 photodetectors; sample device AFM and thickness calibration with applied *E*-field penetration depths simulations (Figure S1); section S.2, method for estimate PC-IQE from the raw PC-signal; section S.3, raw ultrafast-PC trace data for different applied voltages (Figure S2); section S.4, fluence-dependent transient reflectivity response for the fast (γ_f) and slow (γ_s) limits for Auger recombination (Figure S3) (PDF)

Special Issue Paper

This paper was intended for the Toward Chemistry in Real Space and Real Time Virtual Special Issue, published May 14, 2020.

https://dx.doi.org/10.1021/acs.jpcc.0c02646
J. Phys. Chem. C 2020, 124, 15195−15204

AUTHOR INFORMATION

Corresponding Author

Matt W. Graham − *Department of Physics, Oregon State University, Corvallis, Oregon 97331, United States;* orcid.org/0000-0001-6838-3659; Email: graham@physics.oregonstate.edu

Authors

Kyle T. Vogt − *Department of Physics, Oregon State University, Corvallis, Oregon 97331, United States*

Su-Fei Shi − *Department of Chemical Engineering, Rensselaer Polytechnic Institute, Troy, New York 12180, United States;* orcid.org/0000-0001-5158-805X

Feng Wang − *Department of Physics, University of California, Berkeley, California 94720, United States*

Complete contact information is available at: https://pubs.acs.org/10.1021/acs.jpcc.0c02646

Notes

The authors declare no competing financial interest.

ACKNOWLEDGMENTS

This work acknowledges the Spectroscopy Society of Pittsburgh Starter Grant, NSF MRI grant 1920368, and Oregon Best for project support. S.-F. Shi acknowledges support by AFOSR through grant No. FA9550-18-1-0321.

REFERENCES

(1) Yu, W. J.; Liu, Y.; Zhou, H.; Yin, A.; Li, Z.; Huang, Y.; Duan, X. *Nat. Nanotechnol.* **2013**, *8*, 952−958.

(2) Massicotte, M.; Schmidt, P.; Vialla, F.; Schädler, K. G.; Reserbat-Plantey, A.; Watanabe, K.; Taniguchi, T.; Tielrooij, K. J.; Koppens, F. H. L. *Nat. Nanotechnol.* **2016**, *11*, 42−46.

(3) Lee, C.-H.; Lee, G.-H.; van der Zande, A. M.; Chen, W.; Li, Y.; Han, M.; Cui, X.; Arefe, G.; Nuckolls, C.; Heinz, T. F.; Guo, J.; Hone, J.; Kim, P. *Nat. Nanotechnol.* **2014**, *9*, 676−681.

(4) Huang, C.; Wu, S.; Sanchez, A. M.; Peters, J. J. P.; Beanland, R.; Ross, J. S.; Rivera, P.; Yao, W.; Cobden, D. H.; Xu, X. *Nat. Mater.* **2014**, *13*, 1096−1101.

(5) Vogt, K.; Shi, S.; Wang, F.; Graham, M. W. Dynamic Resolution of Photocurrent Generating Pathways by Field-Dependent Ultrafast Microscopy; *International Conference on Ultrafast Phenomena*; OSA, 2016; p UW2A.3.

(6) Zhou, X.; Hu, X.; Zhou, S.; Song, H.; Zhang, Q.; Pi, L.; Li, L.; Li, H.; Lü, J.; Zhai, T. *Adv. Mater.* **2018**, *30*, 1703286.

(7) Zipfel, J.; Kulig, M.; Perea-Causín, R.; Brem, S.; Ziegler, J. D.; Rosati, R.; Taniguchi, T.; Watanabe, K.; Glazov, M. M.; Malic, E.; Chernikov, A. *Phys. Rev. B: Condens. Matter Mater. Phys.* **2020**, *101*, 115430.

(8) Selig, M.; Katsch, F.; Schmidt, R.; Michaelis de Vasconcellos, S.; Bratschitsch, R.; Malic, E.; Knorr, A. *Physical Review Research* **2019**, *1*, 022007.

(9) Zhao, W.; Ghorannevis, Z.; Chu, L.; Toh, M.; Kloc, C.; Tan, P.-H.; Eda, G. *ACS Nano* **2013**, *7*, 791−797.

(10) Mueller, T.; Malic, E. *npj 2D Materials and Applications* **2018**, *2*, 29.

(11) Wang, H.; Zhang, C.; Rana, F. *Nano Lett.* **2015**, *15*, 339−345.

(12) Strait, J. H.; Nene, P.; Rana, F. *Phys. Rev. B: Condens. Matter Mater. Phys.* **2014**, *90*, 245402.

(13) Moody, G.; Schaibley, J.; Xu, X. *J. Opt. Soc. Am. B* **2016**, *33*, C39.

(14) Yuan, L.; Huang, L. *Nanoscale* **2015**, *7*, 7402−7408.

(15) Li, Y.; Shi, J.; Chen, H.; Wang, R.; Mi, Y.; Zhang, C.; Du, W.; Zhang, S.; Liu, Z.; Zhang, Q.; Qiu, X.; Xu, H.; Liu, W.; Liu, Y.; Liu, X. *Nanoscale* **2018**, *10*, 17585−17592.

(16) Yu, Y.; Yu, Y.; Xu, C.; Barrette, A.; Gundogdu, K.; Cao, L. *Phys. Rev. B: Condens. Matter Mater. Phys.* **2016**, *93*, 201111.

(17) He, C.; Zhu, L.; Zhao, Q.; Huang, Y.; Yao, Z.; Du, W.; He, Y.; Zhang, S.; Xu, X. *Adv. Opt. Mater.* **2018**, *6*, 1800290.

(18) Wang, H.; Zhang, C.; Chan, W.; Tiwari, S.; Rana, F. *Nat. Commun.* **2015**, *6*, 8831.

(19) Merkl, P.; Mooshammer, F.; Steinleitner, P.; Girnghuber, A.; Lin, K.-Q.; Nagler, P.; Holler, J.; Schüller, C.; Lupton, J. M.; Korn, T.; Ovesen, S.; Brem, S.; Malic, E.; Huber, R. *Nat. Mater.* **2019**, *18*, 691−696.

(20) Graham, M. W.; Shi, S.-F.; Wang, Z.; Ralph, D. C.; Park, J.; McEuen, P. L. *Nano Lett.* **2013**, *13*, 5497−5502.

(21) Gabor, N. M.; Zhong, Z.; Bosnick, K.; McEuen, P. L. *Phys. Rev. Lett.* **2012**, *108*, 87404.

(22) Hartland, G. V. *Chemical Science* **2010**, *1*, 303.

(23) Ceballos, F.; Zhao, H. *Adv. Funct. Mater.* **2017**, *27*, 1604509.

(24) Patel, H.; Havener, R. W.; Brown, L.; Liang, Y.; Yang, L.; Park, J.; Graham, M. W. *Nano Lett.* **2015**, *15*, 5932−5937.

(25) Vialla, F.; Danovich, M.; Ruiz-Tijerina, D. A.; Massicotte, M.; Schmidt, P.; Taniguchi, T.; Watanabe, K.; Hunt, R. J.; Szyniszewski, M.; Drummond, N. D.; Pedersen, T. G.; Fal'ko, V. I.; Koppens, F. H. L. *2D Mater.* **2019**, *6*, 035032.

(26) Poellmann, C.; Steinleitner, P.; Leierseder, U.; Nagler, P.; Plechinger, G.; Porer, M.; Bratschitsch, R.; Schüller, C.; Korn, T.; Huber, R. *Nat. Mater.* **2015**, *14*, 889−893.

(27) Yuan, L.; Wang, T.; Zhu, T.; Zhou, M.; Huang, L. Exciton Dynamics, Transport, and Annihilation in Atomically Thin Two-Dimensional Semiconductors. *J. Phys. Chem. Lett.* **2017**, *8*, 3371−3379.

(28) Graham, M. W.; Shi, S.-F.; Ralph, D. C.; Park, J.; McEuen, P. L. *Nat. Phys.* **2013**, *9*, 103−108.

(29) Kim, D.; Du, H.; Kim, T.; Shin, S.; Kim, S.; Song, M.; Lee, C.; Lee, J.; Cheong, H.; Seo, D. H.; Seo, S. *AIP Adv.* **2016**, *6*, 105307.

(30) Moody, G.; Tran, K.; Lu, X.; Autry, T.; Fraser, J. M.; Mirin, R. P.; Yang, L.; Li, X.; Silverman, K. L. *Phys. Rev. Lett.* **2018**, *121*, 057403.

(31) Cui, Q.; Ceballos, F.; Kumar, N.; Zhao, H. *ACS Nano* **2014**, *8*, 2970−2976.

(32) Zhu, S.; Li, D.; Hu, Y.; Wang, J.; Wang, X.; Lu, W. *Mater. Res. Express* **2018**, *5*, 066209.

(33) Kaviraj, B.; Sahoo, D. *RSC Adv.* **2019**, *9*, 25439−25461.

(34) Pogna, E. A. A.; Marsili, M.; De Fazio, D.; Dal Conte, S.; Manzoni, C.; Sangalli, D.; Yoon, D.; Lombardo, A.; Ferrari, A. C.; Marini, A.; Cerullo, G.; Prezzi, D. *ACS Nano* **2016**, *10*, 1182−1188.

(35) Koperski, M.; Nogajewski, K.; Arora, A.; Cherkez, V.; Mallet, P.; Veuillen, J.-Y.; Marcus, J.; Kossacki, P.; Potemski, M. *Nat. Nanotechnol.* **2015**, *10*, 503−506.

(36) He, Y.-M.; Clark, G.; Schaibley, J. R.; He, Y.; Chen, M.-C.; Wei, Y.-J.; Ding, X.; Zhang, Q.; Yao, W.; Xu, X.; Lu, C.-Y.; Pan, J.-W. *Nat. Nanotechnol.* **2015**, *10*, 497−502.

(37) Ovesen, S.; Brem, S.; Linderälv, C.; Kuisma, M.; Korn, T.; Erhart, P.; Selig, M.; Malic, E. *Communications Physics* **2019**, *2*, 23.

(38) Amani, M.; et al. *Science* **2015**, *350*, 1065−1068.

(39) Borzda, T.; Gadermaier, C.; Vujicic, N.; Topolovsek, P.; Borovsak, M.; Mertelj, T.; Viola, D.; Manzoni, C.; Pogna, E. A. A.; Brida, D.; Antognazza, M. R.; Scotognella, F.; Lanzani, G.; Cerullo, G.; Mihailovic, D. *Adv. Funct. Mater.* **2015**, *25*, 3351−3358.

(40) Yu, Y.; Yu, Y.; Xu, C.; Barrette, A.; Gundogdu, K.; Cao, L. *Phys. Rev. B: Condens. Matter Mater. Phys.* **2016**, *93*, 201111.

(41) Arora, A.; Koperski, M.; Nogajewski, K.; Marcus, J.; Faugeras, C.; Potemski, M. Excitonic resonances in thin films of WSe_2: from monolayer to bulk material. *Nanoscale* **2015**, *7*, 10421.

(42) Mouri, S.; Miyauchi, Y.; Toh, M.; Zhao, W.; Eda, G.; Matsuda, K. *Phys. Rev. B: Condens. Matter Mater. Phys.* **2014**, *90*, 155449.

(43) Rivera, P.; Schaibley, J. R.; Jones, A. M.; Ross, J. S.; Wu, S.; Aivazian, G.; Klement, P.; Seyler, K.; Clark, G.; Ghimire, N. J.; Yan, J.; Mandrus, D. G.; Yao, W.; Xu, X. *Nat. Commun.* **2015**, *6*, 6242.

(44) Sun, D.; Rao, Y.; Reider, G. A.; Chen, G.; You, Y.; Brézin, L.; Harutyunyan, A. R.; Heinz, T. F. *Nano Lett.* **2014**, *14*, 5625−5629.

(45) Zhao, W.; Ghorannevis, Z.; Chu, L.; Toh, M.; Kloc, C.; Tan, P.-H.; Eda, G. *ACS Nano* **2013**, *7*, 791−797.

(46) Massicotte, M.; Schmidt, P.; Vialla, F.; Watanabe, K.; Taniguchi, T.; Tielrooij, K. J.; Koppens, F. H. L. *Nat. Commun.* **2016**, *7*, 12174.

(47) Wu, J.; Fan, Z.; Chen, J.; Jiang, X. *Appl. Phys. Express* **2018**, *11*, 054001.
(48) Fang, H.; et al. *Proc. Natl. Acad. Sci. U. S. A.* **2014**, *111*, 6198−6202.
(49) Kim, D.; Du, H.; Kim, T.; Shin, S.; Kim, S.; Song, M.; Lee, C.; Lee, J.; Cheong, H.; Seo, D. H.; Seo, S. *AIP Adv.* **2016**, *6*, 105307.
(50) Palummo, M.; Bernardi, M.; Grossman, J. C. *Nano Lett.* **2015**, *15*, 2794−2800.
(51) Cui, Q.; Ceballos, F.; Kumar, N.; Zhao, H. *ACS Nano* **2014**, *8*, 2970−2976.
(52) Bakulin, A. A.; Silva, C.; Vella, E. *J. Phys. Chem. Lett.* **2016**, *7*, 250−258.

https://dx.doi.org/10.1021/acs.jpcc.0c02646
J. Phys. Chem. C 2020, 124, 15195−15204